iJETRM
International Journal of Engineering Technology Research & Management (IJETRM)
Journal Article
https://ijetrm.com/issue/

ENHANCING THE CRYSTALLIZATION OF LEAD-FREE $CS_3BI_2I_9$ MATERIAL USING CONTROLLED THERMAL ANNEALING AND ITS ROLE IN PHOTOVOLTAIC PERFORMANCE: A COMPUTATIONAL AND EXPERIMENTAL INVESTIGATION

Ambreesh Kumar[1], Ravindra Kumar Rawat[1]*, Praveen Kumar Prajapati[1], Anil Kumar Sharma[1], Jitendra Yadav[1] and Dhirendra Kumar Chaudhary[1]*
[1]Centre for Renewable Energy, Prof. Rajendra Singh (Rajju Bhaiya),
Institute of Physical Sciences for Study and Research,
VBS Purvanchal University, Jaunpur, Uttar Pradesh, India–222003
Corresponding Authors:
Ravindra Kumar Rawat
rkau007@gmail.com
https://orcid.org/0000-0003-2594-9362

ABSTRACT
Lead-free $Cs_3Bi_2I_9$ thin films were synthesized and annealed at 80 to 110 °C to investigate structural and optical properties for photovoltaic applications. X-ray diffraction confirms phase-pure hexagonal $Cs_3Bi_2I_9$ (P63/mmc), with crystallite size increases as annealing temperature rises, indicating improved crystallinity and reduced defects. The density-functional-theory calculations reveal a semiconducting bandgap of 2.07 eV. The material shows a high refractive index (3.03), low reflectivity (<0.4), and large absorption coefficient, enabling efficient light harvesting. Enhanced dielectric response and optical conductivity further support strong photo-induced carrier generation. Improved morphology and favorable optoelectronic properties establish $Cs_3Bi_2I_9$ as a stable, non-toxic absorber for perovskite solar cells.

Keywords:
$Cs_3Bi_2I_9$; Computational; Solar Cell; Refractive Index; Dielectric;

1. INTRODUCTION

Halide perovskites have rapidly advanced as next-generation absorber materials for photovoltaic technologies owing to their outstanding optoelectronic properties and solution-processable fabrication [1, 2]. Since their first implementation in solar cells, power-conversion efficiencies have increased dramatically, positioning perovskites as strong alternatives to conventional silicon and thin-film semiconductors [3]. Among them, all-inorganic and hybrid compositions such as $Cs_3Bi_2I_9$ and $CH_3NH_3PbI_3$ offer favorable band gaps, high absorption coefficients, long carrier diffusion lengths, and defect tolerance attributes that are essential for efficient light harvesting and charge transport in solar-energy devices [2, 4]. Their tunable chemistry enables precise control over electronic structure and optical response, allowing optimization across the solar spectrum [4]. A defining advantage of perovskite absorbers is their strong interaction with visible and near-infrared radiation. High refractive indices and large extinction coefficients promote effective optical confinement and enhanced photon absorption within thin films, reducing material consumption while maintaining high photocurrent generation [4, 5]. Furthermore, the dielectric screening in these materials suppresses non-radiative recombination, supporting long carrier lifetimes and efficient charge separation [6-8]. The ability to tailor the bandgap through halide substitution or cation engineering enables compositional tuning from the near-infrared to visible region, facilitating single-junction and tandem solar-cell architectures [9-11]. Lead-free variants such as bismuth-based perovskites have also attracted attention as environmentally benign alternatives with improved chemical stability [2, 12].

The optoelectronic properties of halide perovskites are strongly governed by thermal annealing in the 80-110 °C range, which controls crystallization, lattice ordering, and defect density [13, 14]. Lower annealing temperatures

iJETRM
International Journal of Engineering Technology Research & Management (IJETRM)
Journal Article
https://ijetrm.com/issue/

(~80 °C) often yield incomplete crystal growth and higher defect concentrations, whereas optimized annealing near 100-110 °C promotes phase stabilization, larger grains, and reduced trap states, thereby enhancing carrier mobility, optical absorption, and photovoltaic performance [14].

Density functional theory (DFT) provides atomistic understanding of the intrinsic electronic structure and defect energetics of perovskites, including band dispersion, dielectric response, and optical transitions [15-18]. Such theoretical insights clarify how reduced defect density and improved lattice ordering lead to lower recombination losses and stronger light-matter interaction in well-crystallized films. Overall, the synergy between optimized thermal annealing, improved crystallinity, and favorable electronic structure is essential for achieving stable, high-efficiency perovskite solar cells. Combining controlled film formation with theoretical guidance remains a key strategy for advancing perovskite photovoltaic technologies [19-20].

2. EXPERIMENTAL METHODS

2.1 Materials:

Cesium iodide (CsI, 99.9% trace metals basis) and bismuth iodide (BiI_3, 99.9% trace metals basis) were used as precursor salts for $Cs_3Bi_2I_9$ thin-film preparation. N,N-dimethylformamide (DMF, anhydrous, 99.8%) served as the solvent for dissolving the metal halides and forming a homogeneous precursor solution. Fluorine-doped tin oxide (FTO) coated glass substrates (sheet resistance ~15 Ω/sq) were employed as conductive substrates for film deposition. All chemicals and substrates were purchased from Merck (Sigma-Aldrich) and used as received without further purification. Deionized (DI) water, acetone, and ethanol (analytical grade, 99.5%, Merck Sigma-Aldrich) were used for substrate cleaning prior to deposition.

2.2 Fabrication of $Cs_3Bi_2I_9$ thin films and annealing at various temperatures:

The $Cs_3Bi_2I_9$ thin films were fabricated on FTO glass substrates using a conventional spin-coating route followed by thermal annealing at different temperatures (Figure 1). Initially, a precursor solution was prepared by dissolving cesium iodide (CsI) and bismuth iodide (BiI_3) in dimethylformamide (DMF) with a molar ratio of 3:2, ensuring complete dissolution under magnetic stirring to obtain a homogeneous solution. The FTO substrates were thoroughly cleaned, typically by sequential ultrasonication in detergent, deionized water, acetone, and ethanol, and then dried to remove surface contaminants. A measured volume of the precursor solution was dropped onto the cleaned FTO substrate and spin-coated at 1000 rpm for 30 s to form a uniform wet film. The coated films were subsequently annealed at various temperatures (80 °C, 90 °C, 100 °C, and 110 °C) to promote solvent evaporation, crystallization, and phase formation of $Cs_3Bi_2I_9$, enabling investigation of temperature-dependent structural and optical properties.

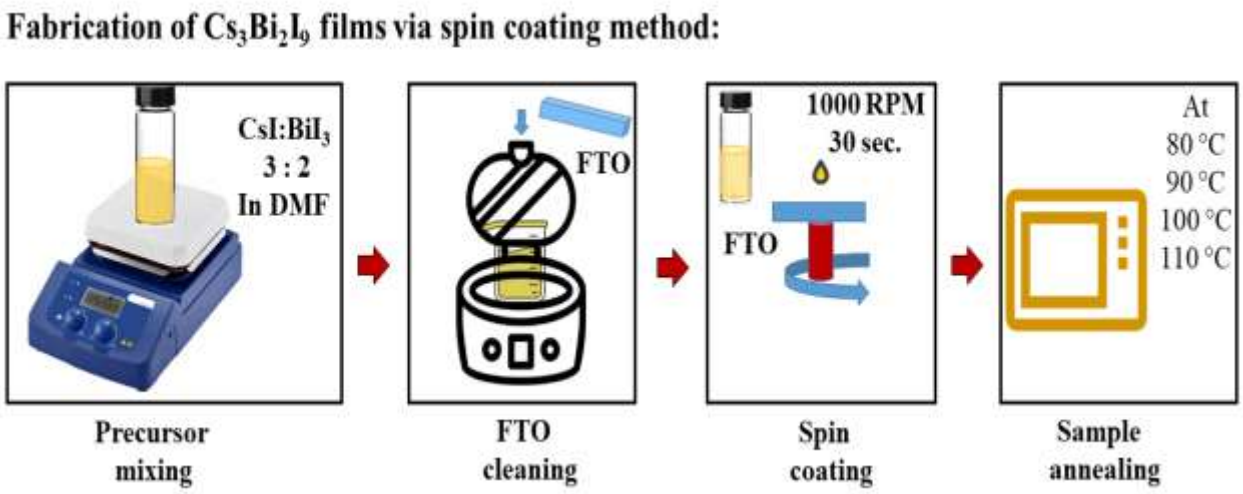

Figure 1: Schematic of $Cs_3Bi_2I_9$ film fabrication on FTO via spin coating (1000 rpm, 30 s) method, and annealing at 80-110 °C.

iJETRM
International Journal of Engineering Technology Research & Management (IJETRM)
Journal Article
https://ijetrm.com/issue/

3. COMPUTATIONAL DETAILS:

The computational investigation of the $Cs_3Bi_2I_9$ perovskite was performed using density functional theory (DFT) within the CASTEP module of Materials Studio [1, 19]. Norm-conserving pseudopotentials generated under the PBE exchange-correlation functional were employed for Cs, Bi, and I atoms, with relativistic effects treated using the Koelling–Harmon approach. A plane-wave basis set with a cutoff energy of 190.5 eV and a 2 × 2 × 2 Monkhorst–Pack k-point grid was used for Brillouin-zone sampling. The hexagonal crystal structure (space group P63/mmc) contained 28 atoms per unit cell with lattice parameters a = b = 8.404 Å and c = 21.183 Å. Self-consistent field calculations were converged to 2×10^{-6} eV per atom. The optimized structure yielded a total energy of −20592.85 eV, confirming stability. These parameters ensured reliable evaluation of the electronic and optical properties of $Cs_3Bi_2I_9$ for photovoltaic applications.

4. RESULT AND DISCUSSION

4.1 Characterization:

Figure 2 presents an X-ray Diffraction (XRD) pattern of a $Cs_3Bi_2I_9$ films. The XRD patterns for the $Cs_3Bi_2I_9$ samples demonstrate high crystallinity and phase purity across all studied annealing temperatures from 80 ℃ to 110 ℃. The diffraction profiles are dominated by a series of sharp, intense peaks, most notably the primary peak at approximately 2θ = 25.21, corresponding to the (003) crystallographic plane. Other significant reflections observed include the (002) plane at 2θ ~ 16.72, the (004) plane at 2θ ~ 37.79, and the (006) plane at 2θ ~ 51.75. All observed diffraction peaks are in excellent agreement with the standard JCPDS card no. 43-0499. This card corresponds to the hexagonal phase of $Cs_3Bi_2I_9$ within the P63/mmc space group. The match confirms that the material is phase-pure and that the low-temperature annealing process successfully facilitates the formation of the desired perovskite-like structure, without secondary phases or degradation products such as BiI_3 or CsI.

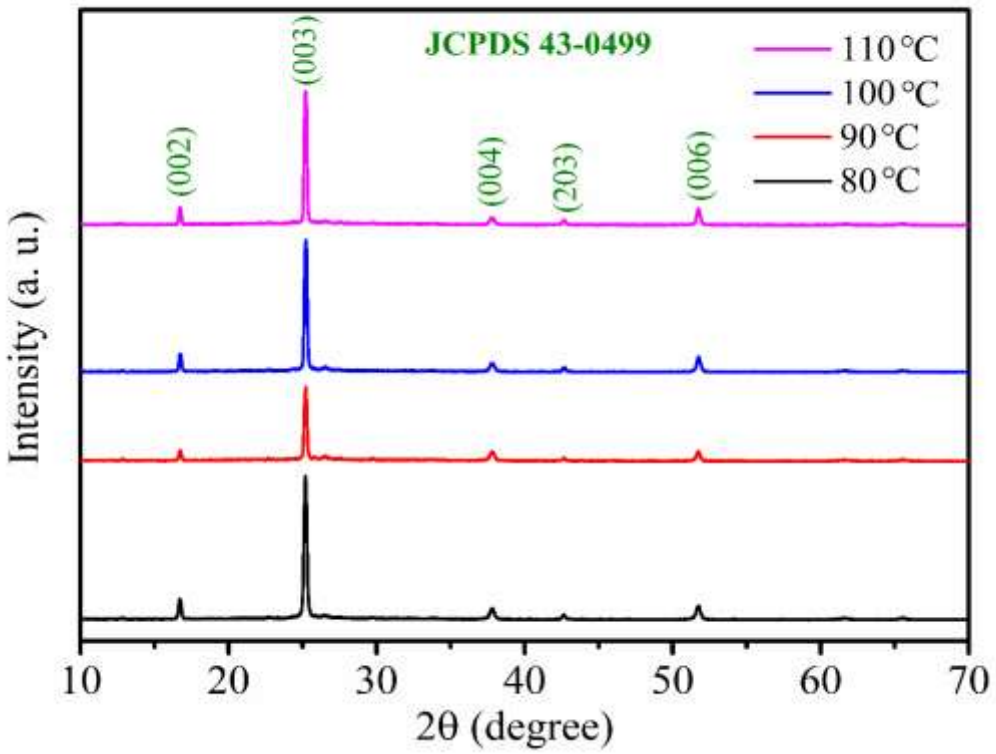

Figure 2. XRD patterns of $Cs_3Bi_2I_9$ samples at various annealing temperatures.

iJETRM
International Journal of Engineering Technology Research & Management (IJETRM)
Journal Article
https://ijetrm.com/issue/

The analysis of the average crystallite size for the $Cs_3Bi_2I_9$ thin films reveals a progressive enhancement in structural quality as a function of thermal treatment. At an initial annealing temperature of 80 ℃, the material exhibits an average crystallite size of approximately 31.29 nm. As the temperature is increased to 90 ℃ and 100 ℃, the crystallite size grows to 33.30 nm and 33.77 nm, respectively, indicating that the thermal energy facilitates the coalescing of smaller grains into larger crystalline domains. The most significant growth is observed at 110 ℃, where the average crystallite size reaches 35.43 nm. This upward trend, derived from the FWHM values of the characteristic diffraction peaks using the Scherrer equation, suggests that higher annealing temperatures reduce lattice strain and defect density, thereby improving crystallinity, which is essential for efficient charge transport in solar cell applications [1].

Tauc plot (Figure 3) for the $Cs_3Bi_2I_9$ samples reveals how different annealing temperatures affect the material's light absorption across the 350 nm to 800 nm range. All four samples exhibit distinct excitonic absorption features, most notably the prominent peaks near 420 nm and 510 nm, characteristic of electronic transitions in this specific bismuth-based perovskite structure.

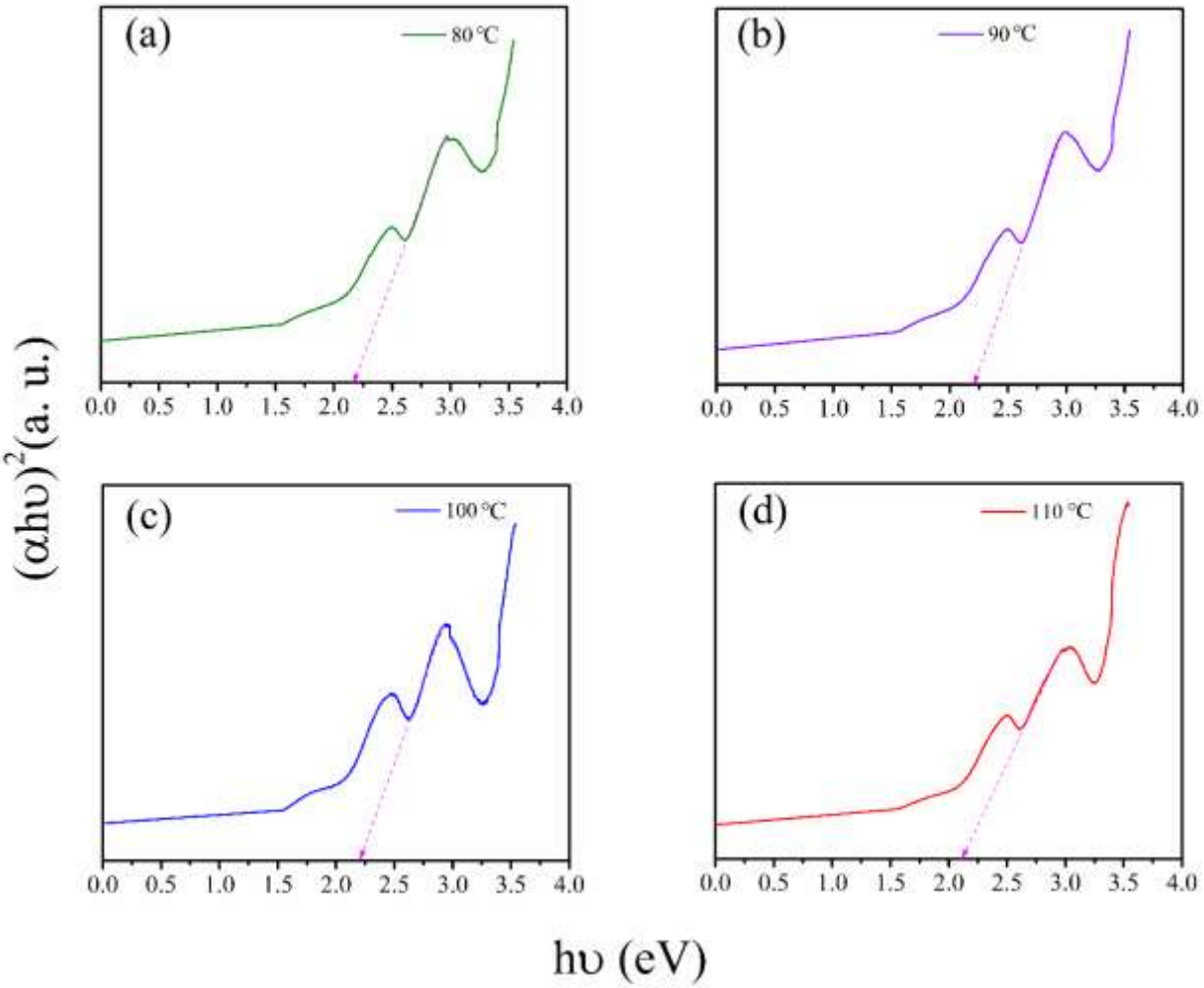

Figure 3. Tauc plot of $Cs_3Bi_2I_9$ thin films at various annealing temperatures.

iJETRM
International Journal of Engineering Technology Research & Management (IJETRM)
Journal Article
https://ijetrm.com/issue/

As the wavelength increases beyond 550 nm, a sharp decline in absorbance is observed, marking the transition toward the optical band gap where the material becomes less efficient at absorbing photons. The sample annealed at 80°C demonstrates the strongest optical response, maintaining the highest absorbance values across the entire measured spectrum. In contrast, the sample annealed at 90°C exhibits the lowest absorbance, rising only slightly above the baseline. The 100°C and 110°C samples fall between these two extremes, with the 110°C sample showing a recovery in absorption intensity compared to the 100°C version. The energy band gaps for the $Cs_3Bi_2I_9$ films are estimated at 2.15 eV (80°C), 2.19 eV (90°C), 2.20 eV (100°C), and 2.11 eV (110°C) based on the Tauc plot intersections.

4.2 Computational results and discussion:

Figure 4(a) shows the crystal structure of $Cs_3Bi_2I_9$ visualized using VESTA. The structure consists of face-sharing BiI_6 octahedra forming $Bi_2I_9^{3-}$ bioctahedral units, which are separated by Cs^+ cations. Unlike conventional three-dimensional perovskites, $Cs_3Bi_2I_9$ exhibits a zero-dimensional structure in which the Bi_2I_9 clusters are structurally isolated from one another. The green spheres represent Cs atoms, the blue spheres represent Bi atoms, and the red spheres represent I atoms. The isolation of the bioctahedra leads to reduced structural connectivity and strong localized Bi-I bonding within the clusters.

Figure 4(b) presents the partial density of states (PDOS) of $Cs_3Bi_2I_9$ calculated using the CASTEP module in Materials Studio. The vertical dashed line at 0 eV represents the Fermi level. The absence of electronic states at the Fermi level indicates that $Cs_3Bi_2I_9$ is a semiconductor with a band gap of 2.07 eV. The valence band region is mainly dominated by iodine 5p orbitals with slight hybridization from bismuth states, whereas the conduction band is primarily contributed by Bi 6p orbitals. The s and d orbitals contribute minimally near the band edges, and the f states are negligible. The sharp peaks observed in the DOS reflect the localized electronic states arising from the zero-dimensional crystal structure. Overall, the electronic structure indicates strong Bi–I orbital hybridization and confirms the semiconducting nature of $Cs_3Bi_2I_9$.

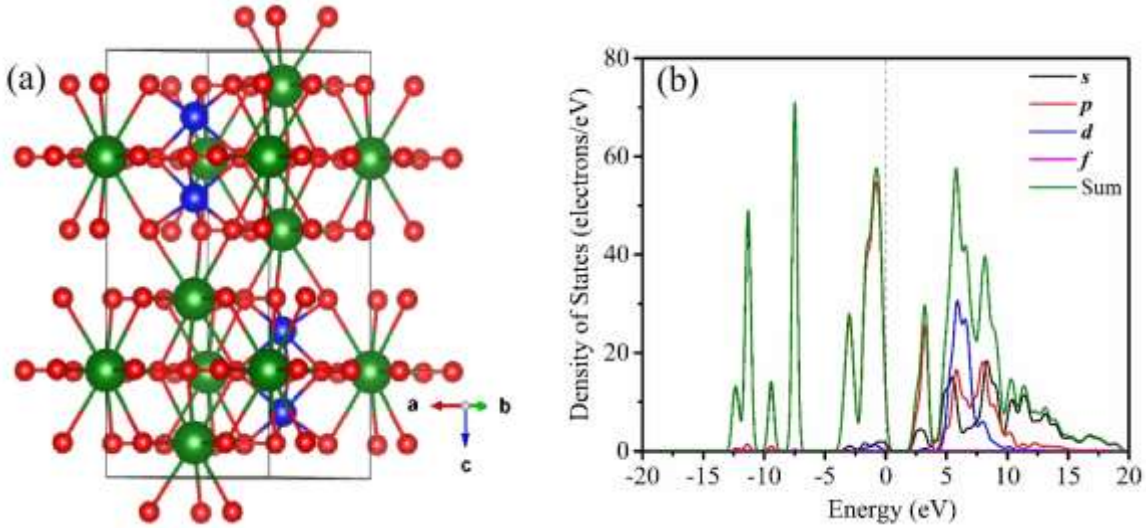

Figure 4: (a) Structural representations of $Cs_3Bi_2I_9$ material generated using VESTA software and (b) Partial density of states (PDOS) calculated using CASTEP.

In solar cells, several fundamental optical properties govern light interaction and determine how efficiently incident photons are absorbed and converted into electrical energy. These include the refractive index, reflectivity, absorption coefficient, energy loss function, and dielectric function, all of which play vital roles in optimizing light harvesting and overall device performance.

The refractive index, $n(\omega)$, is a fundamental optical parameter that describes the reduction in light velocity as it propagates through a material. It is calculated using Equation 1, which links the refractive index to the real $\varepsilon_1(\omega)$ and imaginary $\varepsilon_2(\omega)$ components of the dielectric function. Both dielectric terms are frequency-dependent and vary

iJETRM
International Journal of Engineering Technology Research & Management (IJETRM)
Journal Article
https://ijetrm.com/issue/

with the angular frequency of the incident electromagnetic radiation [1, 19].

$$n(\omega) = [\varepsilon_1(\omega)/2 + \{\varepsilon_1(\omega)^2 + \varepsilon_2(\omega)^2\}^{1/2}/2]^{1/2} \quad (1)$$

Figure 5(a) shows the real (blue) and imaginary (red) parts of the refractive index of $Cs_3Bi_2I_9$ as a function of photon energy. The real part of the refractive index, $n(\omega)$, represents the material's light propagation behavior, while the imaginary part, corresponds to optical absorption and attenuation within the material. In the low-energy (visible) region, the real part exhibits a maximum value of about 3.03 at 2.78 eV, indicating strong light-matter interaction and good optical confinement. A high refractive index in this region enhances light trapping within the absorber layer, thereby improving photon absorption. The imaginary part shows a prominent peak at approximately 1.56 eV (4.13 eV), indicating strong interband electronic transitions and efficient absorption in the near-UV region.

Reflectivity ($R(\omega)$), determined from Equation 2, describes the extent to which a material reflects incident light. In fiber-optic communication systems, reducing reflection is particularly important at connectors and splices, where unwanted reflections can lead to signal loss and degradation. Nevertheless, reflection cannot be completely eliminated, as it naturally occurs at material interfaces due to Fresnel reflection. The reflectivity of a material is therefore evaluated using the standard relation [1]:

$$R(\omega) = (n + ik - 1)/(n + ik + 1) \quad (2)$$

$R(\omega)$ represents how strongly a material surface reflects incoming electromagnetic radiation. Its value lies between 0 and 1, with values closer to 1 indicating stronger reflection. This parameter varies with the angular frequency (ω) of the incident light. Reflectivity is governed by the material's complex refractive index, expressed as ($n + ik$). In this expression, 'n'denotes the real component, which determines the phase velocity of light in the medium, while 'k' is the imaginary component, known as the extinction coefficient, indicating the degree of optical absorption within the material.

Figure 5 (b) illustrates the variation of optical reflectivity, $R(\omega)$, of $Cs_3Bi_2I_9$ as a function of photon energy. In the low-energy region (0-5 eV), the material shows moderate reflectivity, gradually increasing due to the onset of interband electronic transitions. Between 5 and 15 eV, several peaks and dips appear, indicating multiple electronic transitions within the material's band structure. A pronounced maximum reflectivity of about 0.34 occurs at approximately 16.39 eV, corresponding to strong interband excitations. Around 12 eV, a noticeable minimum suggests enhanced absorption and reduced reflection. Beyond 20 eV, the reflectivity sharply decreases and approaches nearly zero at higher energies (above 30 eV), indicating weak reflection in this region. Overall, the reflectivity remains below 0.4 across the studied energy range, demonstrating that $Cs_3Bi_2I_9$ is generally a low-reflective material. This behavior is favorable for optoelectronic and photovoltaic applications, where reduced reflection enhances light absorption efficiency.

The absorption coefficient ($\alpha(\omega)$), calculated from Equation 3, quantifies the extent to which a material absorbs light, resulting in a decrease in the intensity of the transmitted signal. The absorbance of the materials is determined using the standard formula [23]:

$$\alpha(\omega) = (2)^{1/2}\omega[\{\varepsilon_1(\omega)^2 + \varepsilon_2(\omega)^2\}^{1/2} - \varepsilon_1(\omega)]^{1/2} \quad (3)$$

Figure 5(c) shows the computed absorption coefficient (cm^{-1}) as a function of photon energy (eV), illustrating how the material interacts with electromagnetic radiation across a wide spectral range. Absorption is negligible at very low energies (< ~2 eV), indicating transparency in the infrared-near-visible region and suggesting a finite band gap. A sharp rise begins around 3-5 eV, marking the onset of interband electronic transitions from the valence to conduction bands. Several pronounced peaks appear between ~6 and 18 eV, corresponding to strong optical transitions involving deeper valence states and higher conduction states. The dominant peak at 14.34 eV with an absorption of ~2.53×10^5 cm^{-1} signifies the highest probability of photon absorption and reflects a high joint density of states and transition matrix elements at this energy. Beyond ~20 eV, absorption decreases rapidly, with only weak features near 23-26 eV, indicating fewer allowed transitions.

The dielectric function, ($\varepsilon(\omega)$), is a key intrinsic property that characterizes how a material responds to an applied electric field. It is expressed as a complex quantity that depends on the angular frequency of the incident electromagnetic field. Mathematically, the dielectric function can be represented as [1, 19]:

$$\varepsilon(\omega) = \varepsilon_1(\omega) + i\varepsilon_2(\omega) \quad (4)$$

Figure 5 (d) illustrates the calculated complex dielectric function of the $Cs_3Bi_2I_9$ material as a function of photon energy, showing both the real part $\varepsilon_1(\omega)$ (blue) and the imaginary part $\varepsilon_2(\omega)$ (red). The imaginary component, $\varepsilon_2(\omega)$, represents optical absorption due to interband electronic transitions. It exhibits a strong peak at about 3.70 eV

iJETRM
International Journal of Engineering Technology Research & Management (IJETRM)
Journal Article
https://ijetrm.com/issue/

with a value of 7.47, indicating the onset of significant optical transitions from the valence band (mainly I-5p states) to the conduction band (Bi-6p states). Additional smaller features between ~5–15 eV correspond to deeper electronic transitions.

The real part, $\varepsilon_1(\omega)$, describes the dispersive response and refractive behavior of the material. It reaches a maximum of 8.84 at 2.61 eV, reflecting strong polarization near the band-edge region. $\varepsilon_1(\omega)$decreases with increasing energy and becomes slightly negative around 12–15 eV, suggesting plasmon-like behavior and high reflectivity in this range. At higher energies (>20 eV), $\varepsilon_2(\omega)$ approaches zero while $\varepsilon_1(\omega)$ stabilizes near unity, indicating reduced polarization and transparency.

Figure 5 (e) presents the calculated complex optical conductivity of the $Cs_3Bi_2I_9$ material as a function of photon energy, showing the real part (blue) and imaginary part (red). The real component represents the dissipative (absorptive) response associated with interband electronic transitions. It rises sharply from near zero at low energy and reaches a maximum value of about 3.41 at 3.81 eV, indicating the onset of strong optical excitation across the band gap. Additional oscillations between ~6-15 eV arise from transitions involving deeper valence states and higher conduction bands.

The imaginary part reflects the reactive or energy-storage response of charge carriers. It shows a negative minimum at 2.87 eV (-2.62), followed by a zero crossing near 4.56 eV and positive values at higher energies, consistent with resonant polarization processes.

The energy loss function, ($L(\omega)$), defined in Equation 5, characterizes the energy dissipated by the material when it interacts with incident electromagnetic radiation. It quantifies the loss of photon energy due to electronic excitations within the medium. The energy loss function is evaluated using the following relation [1, 19]:

$$L(\omega) = -Im(1/\varepsilon(\omega)) = \varepsilon_2(\omega)/(\varepsilon_1(\omega)^2 + \varepsilon_2(\omega)^2) \qquad (5)$$

Figure 5 (f) shows the calculated energy loss function, $L(\omega)$, of the $Cs_3Bi_2I_9$ material as a function of photon energy. The energy loss function represents the energy dissipated by fast electrons or electromagnetic waves as they traverse the material and is closely related to collective electronic excitations (plasmons). At low photon energies (< ~5 eV), the loss function is nearly zero, indicating minimal energy dissipation and weak electronic excitation in this region, consistent with the semiconducting nature of $Cs_3Bi_2I_9$.

As energy increases, several small features appear between ~6 and 12 eV, associated with interband transitions involving valence states mainly derived from I-5p orbitals. A pronounced and dominant peak occurs at 20.67 eV with a maximum value of about 2.77, corresponding to the bulk plasmon resonance of the material, where collective oscillations of valence electrons are strongest. Beyond ~23 eV, the loss function rapidly decreases toward zero, indicating diminished plasmon activity and reduced electronic response.

In conclusion, $Cs_3Bi_2I_9$ has emerged as a promising lead-free perovskite-derived material for photovoltaic applications due to its favorable optical and structural properties. Its high refractive index (~3.03 at 2.78 eV) enables strong light confinement within the absorber layer, enhancing photon harvesting and improving solar-cell efficiency. The material exhibits low reflectivity (<0.4 across the studied range), which minimizes optical losses at the surface and allows greater light penetration into the active layer-an essential requirement for efficient solar absorbers.

The absorption coefficient shows a sharp increase in the near-UV region with very high values (~2.53×10^5 cm^{-1}), indicating strong interband transitions and effective photon absorption capability. The dielectric response further confirms intense polarization and electronic transition activity near the band edge, supporting efficient generation of charge carriers under illumination. Optical conductivity peaks around 3.8 eV demonstrate good photo-induced carrier excitation.

Structurally, thermal annealing enhances crystallite size from ~31 nm to ~35 nm, reducing defects and improving crystallinity. This leads to better charge transport and reduced recombination. Collectively, these properties establish $Cs_3Bi_2I_9$ as a stable, non-toxic, and efficient light-absorbing material suitable for lead-free solar cells.

Moreover, Table 1 provides a comparative overview of selected perovskite materials for solar energy conversion, focusing on refractive index, dielectric constant, and band gap-key parameters governing light absorption and charge separation in photovoltaic devices. The refractive index ranges from 2.30 to 3.03, indicating strong optical confinement, while dielectric constants (4.98-8.48) suggest effective screening of charge carriers. Band gaps span ~1.03-2.13 eV, covering the optimal range for solar harvesting. Rb-based chlorides exhibit narrow gaps suitable for broadband absorption, whereas $CsPbBr_3$ and $Cs_3Bi_2I_9$ show wider gaps and high dielectric response. Notably, $Cs_3Bi_2I_9$ demonstrates the highest refractive index and dielectric constant, highlighting its promise for efficient

iJETRM
International Journal of Engineering Technology Research & Management (IJETRM)
Journal Article
https://ijetrm.com/issue/

perovskite solar cells.

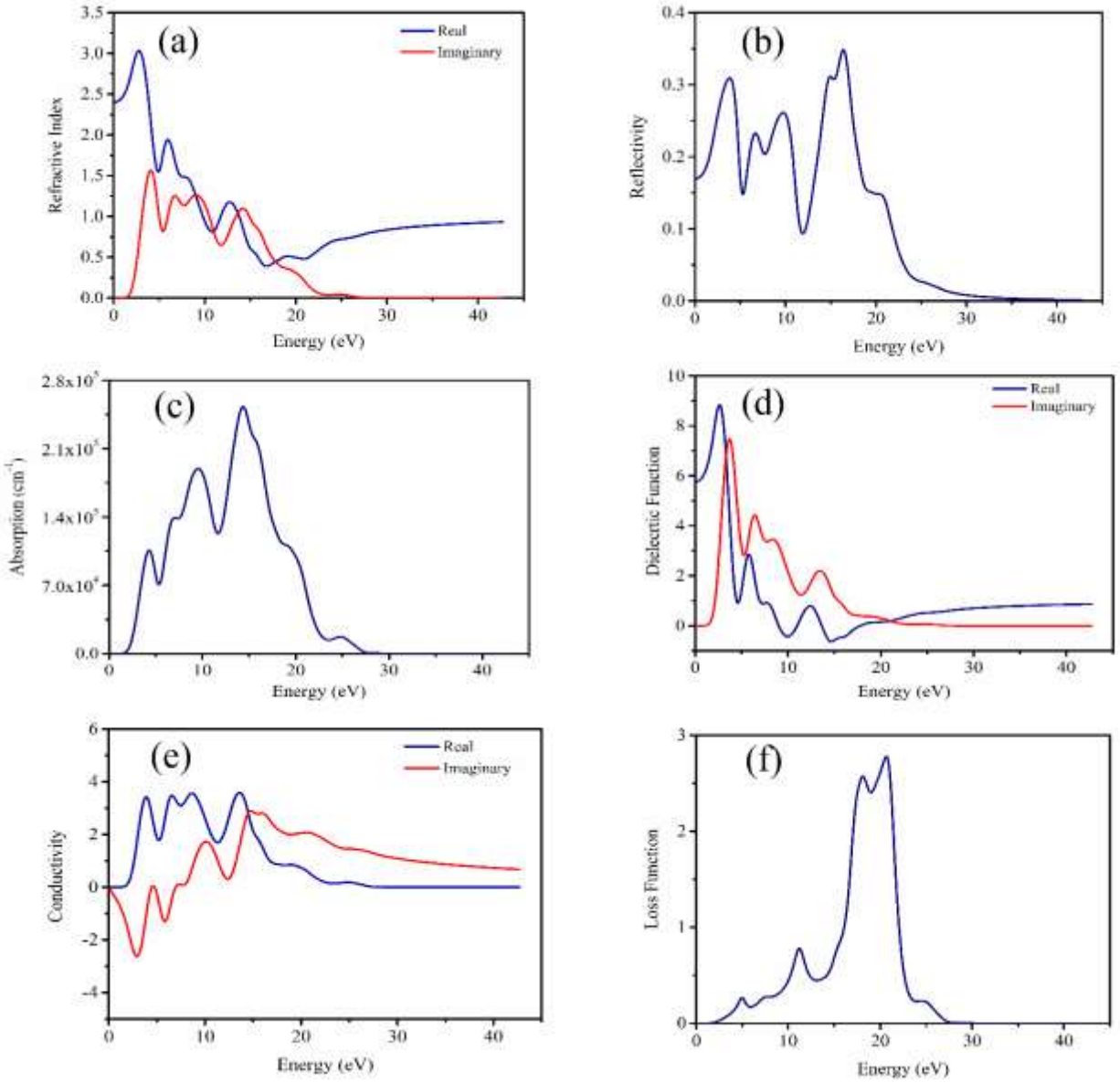

Figure 5. Computed optical response of $Cs_3Bi_2I_9$ as a function of incident photon energy, showing: (a) real and imaginary components of the refractive index; (b) reflectivity; (c) absorption coefficient; (d) real and imaginary parts of the dielectric function; (e) real and imaginary components of optical conductivity; and (f) electron energy-loss function.

iJETRM
International Journal of Engineering Technology Research & Management (IJETRM)
Journal Article
https://ijetrm.com/issue/

Table 1. Comparative summary of perovskite materials for solar-energy conversion based on computational analysis, including compositions and key photovoltaic properties.

Material	Refractive index (n)	Dielectric constant (ε_1)	Band Gap	Ref.
$CsPbBr_3$	2.33	6.77	1.84 eV	[18]
$RbSnCl_3$	2.83	4.98	1.07eV	[19]
$RbGeCl_3$	2.42	5.71	1.03 eV	[19]
$RbPbCl_3$	2.30	5.13	2.13 eV	[19]
$CH_3NH_3PbI_3$	2.61	6.5	-	[20]
$CH_3NH_3PbI_3$	2.84	6.18	1.59 eV	[17]
$Cs_3Bi_2I_9$	3.03	8.48	2.07 eV	**This work**

5. CONCLUSION

In this work, lead-free $Cs_3Bi_2I_9$ thin films were successfully fabricated and annealed at 80-110 °C to evaluate their structural, optical, and electronic properties for photovoltaic applications. X-ray diffraction analysis confirmed the formation of a phase-pure hexagonal $Cs_3Bi_2I_9$ structure without secondary phases, while the progressive increase in crystallite size from 31.29 nm to 35.43 nm with annealing temperature indicated enhanced crystallinity and reduced lattice defects. Such structural improvement promotes efficient charge transport and suppresses recombination losses in solar absorbers. Optical investigations revealed strong excitonic absorption in the visible region and a high absorption coefficient (~10^5 cm^{-1}), demonstrating excellent photon-harvesting capability. The material exhibited a high refractive index (3.03) and low reflectivity (<0.4), ensuring effective light confinement and minimal optical losses. The semiconducting bandgap (2.07 eV), supported by both Tauc analysis and electronic structure calculations, is well suited for visible-light absorption. Additionally, pronounced dielectric response and optical conductivity confirmed strong photo-induced carrier excitation. Overall, the combined improvements in morphology, crystallinity, and optoelectronic performance with moderate annealing establish $Cs_3Bi_2I_9$ as a stable, environmentally benign, and efficient light-absorbing material for lead-free perovskite solar cells.

Acknowledgements
This work was financially supported by the University Grants Commission (UGC), New Delhi, India. The authors gratefully acknowledge additional support from the Department of Science and Technology (DST), Government of India, under the DST-PURSE (SR/PURSE/2024/230) scheme. The research was carried out at the Prof. Rajendra Singh (Rajju Bhaiya) Institute of Physical Sciences for Study and Research, Veer Bahadur Singh Purvanchal University, Jaunpur, India.

Conflict of Interests
The authors declare that they have no conflict of interest.

CRediT Author Contribution
Ambreesh Kumar: Writing-original draft, Formal analysis, Methodology, Investigation, **Ravindra Kumar Rawat:** Writing-original draft, Review and editing, Data curation, Investigation, Validation, Software, **Praveen Kumar Prajapati:** Formal analysis and Methodology, **Anil Kumar Sharma:** Investigation, and Validation, **Jitendra Yadav:** Methodology, Data curation **Dhirendra Kumar Chaudhary:** Validation, Formal analysis, Investigation, Supervision,

Other Authors' E-mail:
Ambreesh Kumar: ambreeshkumar102@gmail.com
Praveen Kumar Prajapati: praveendst825@gmail.com
Anil Kumar Sharma: anilksharma.au@gmail.com
Jitendra Yadav: jit.phy05@gmail.com
Dhirendra Kumar Chaudhary: phydhiren@gmail.com

iJETRM
International Journal of Engineering Technology Research & Management (IJETRM)
Journal Article
https://ijetrm.com/issue/

REFERENCES

1) M. S. Patel, P. Singh, M. K. Singh, S. Yadav, R. K. Rawat, A. Kumar, D. K. Chaudhary, Experimental and computational investigation of $CH_3NH_3PbI_3$ material for next-generation fiber optic applications, Chem. Inorg. Mater. 7 (2025) 100129.
2) J.M. Ball, M.M. Lee, A. Hey, H.J. Snaith, Low-temperature processed meso-superstructured to thin-film perovskite solar cells, Energy Environ. Sci. 6 (2013) 1739–1743.
3) D.W. de Quilettes, S.M. Vorpahl, S.D. Stranks, H. Nagaoka, G.E. Eperon, M.E. Ziffer, H.J. Snaith, D.S. Ginger, Impact of microstructure on local carrier lifetime in perovskite solar cells, Science 348 (2015) 683–686.
4) M.S. Patel, D.K. Chaudhary, P. Kumar, L. Kumar, Fullerene (C_{60})-modulated surface evolution in $CH_3NH_3PbI_3$ and its role in controlling the performance of inverted perovskite solar cells, J. Mater. Sci.: Mater. Electron. 31 (2020) 11150–11158.
5) H. Chen, X. Ding, X. Pan, T. Hayat, A. Alsaedi, Y. Ding, S. Dai, Incorporating C_{60} as nucleation sites optimizing PbI_2 films to achieve perovskite solar cells showing excellent efficiency and stability via vapor-assisted deposition method, ACS Appl. Mater. Interfaces 10 (2017) 2603–2611.
6) W. Qiu, Z. Xiao, K. Roh, N.K. Noel, A. Shapiro, P. Heremans, B.P. Rand, Mixed lead-tin halide perovskites for efficient and wavelength-tunable near-infrared light-emitting diodes, Adv. Mater. 31 (2018).
7) T. Soto-Montero, M. Morales-Masis, Laser deposition of metal halide perovskites, ACS Energy Lett. 9 (2024) 4199–4208.
8) Y. Zhang, B. Li, L. Fu, L. Yin, One-step spin-coating route for homogeneous perovskite/pyrrole-C_{60} fullerene bulk heterojunction for high-performance solar cells, J. Power Sources 419 (2019) 27–34.
9) B.S. Kalanoor, L. Gouda, R. Gottesman, S. Tirosh, E. Haltzi, A. Zaban, Y.R. Tischler, Third-order optical nonlinearities in organometallic methylammonium lead iodide perovskite thin films, ACS Photonics 3 (2016) 361–370.
10) H. Wang, A. Treglia, M.D. Albaqami, F. Gao, A. Petrozza, Tin-halide perovskites for near-infrared light-emitting diodes, ACS Energy Lett. 9 (2024) 2500–2507.
11) H. Wang, Y. Sun, J. Chen, F. Wang, R. Han, C. Zhang, J. Kong, L. Li, J. Yang, A review of perovskite-based photodetectors and their applications, Nanomaterials 12 (2022) 4390.
12) Y. Dang, Y. Liu, Y. Sun, D. Yuan, X. Liu, W. Lu, G. Liu, H. Xia, X. Tao, Bulk crystal growth of hybrid perovskite material $CH_3NH_3PbI_3$, CrystEngComm 17 (2014) 665–670.
13) G. Xing, N. Mathews, S.S. Lim, N. Yantara, X. Liu, D. Sabba, M. Grätzel, S. Mhaisalkar, T.C. Sum, Low-temperature solution-processed wavelength-tunable perovskites, Nat. Mater. 13 (2014) 476–480.
14) C. Bao, J. Yang, S. Bai, W. Xu, Z. Yan, Q. Xu, J. Liu, W. Zhang, F. Gao, High-performance and stable all-inorganic metal-halide perovskite-based photodetectors for optical communication applications, Adv. Mater. 30 (2018).
15) R. Batool, T. Mahmood, A comparative study of cubic methylammonium lead iodide ($CH_3NH_3PbI_3$) perovskite by using density functional theory, Mater. Today Commun. 35 (2023) 105814.
16) I. Abdelwahab, G. Grinblat, K. Leng, Y. Li, X. Chi, A. Rusydi, S.A. Maier, K.P. Loh, Highly enhanced third-harmonic generation in 2D perovskites at excitonic resonances, ACS Nano 12 (2018) 644–650.
17) A. Yang, M. Bai, X. Bao, J. Wang, W. Zhang, Investigation of optical and dielectric constants of organic–inorganic $CH_3NH_3PbI_3$ perovskite thin films, J. Nanomed. Nanotechnol. 7 (2016).
18) Hussain, J.U. Rehman, Investigation of structural, electronic, optical and mechanical properties of perovskite $CsPbBr_3$ material through induced pressure for photovoltaic applications: a DFT insight, Comput. Theor. Chem. (2024).
19) M.U. Ghani, M. Sagir, M.B. Tahir, H. Elsaeedy, S. Nazir, H. Alrobei, M. Alzaid, CASTEP investigation of structural, electronic and optical properties of halide perovskites $RbXCl_3$ (X = Ge, Sn, Pb) for solar cell applications, Inorg. Chem. Commun. 155 (2023) 111007.
20) P. Löper, M. Stuckelberger, B. Niesen, J. Werner, M. Filipič, S. Moon, J. Yum, M. Topič, S. De Wolf, C. Ballif, Complex refractive index spectra of $CH_3NH_3PbI_3$ perovskite thin films determined by spectroscopic ellipsometry and spectrophotometry, J. Phys. Chem. Lett. 6 (2014) 66–71.